# A variable stability projectile using an internal moving mass

**J Rogers** and **M Costello***
School of Aerospace Engineering, Georgia Institute of Technology, Atlanta, Georgia, USA

**Abstract:** Weapon designers have known for some time that projectiles with low static margin have proven to be more susceptible to launch perturbations than comparable projectiles with high static stability, and that low static margin allows greater control authority. The work reported here examines a mechanism for active static margin control in flight through mass centre modification, demonstrating that such a system has significant impact on required manoeuvre control force to achieve a given control authority. A system is developed wherein a mass translates aft during flight inside a cavity aligned with the projectile centre-line, thereby altering the mass centre. This in turn decreases the projectile's static margin after launch and allows greater control authority later in flight, while at the same time decreasing initial throw-off errors. A seven-degree-of-freedom flight dynamic model is used to predict the performance of the system. Results show that by decreasing static margin after launch the projectile is less susceptible to launch perturbations and has increased control authority through the remainder of flight, leading to a smart projectile that outperforms rigid projectiles that are highly stable or highly manoeuvrable. This smart weapon feature is particularly attractive when the maximum control force and moment are small, and therefore is developed specifically for controllable munitions rather than missiles, which often exhibit ample control authority.

**Keywords:** projectile stability, static margin, smart weapons, smart projectiles, variable stability, static stability, control authority

## 1 INTRODUCTION

One of the primary causes of errors for smart weapons is trajectory alterations caused by launch perturbations. These trajectory alterations can be significant in projectiles with low static stability. At the same time, projectiles with higher static margin are less susceptible to launch uncertainties, less manoeuvrable, and require greater control loads to provide trajectory correction. As a result, smart weapon designers are routinely faced with a trade-off when determining centre of gravity location or aerodynamic design. The goal is to protect against launch disturbances while still guaranteeing reasonable force requirements from a control mechanism.

Limited work has been reported examining the effect of mass centre position on impact point errors.

A notable exception is Rollstin [1], who examined the effect of mass centre position on impact point errors with an emphasis on lateral throw-off due to the yaw of repose. There has been substantial research on the effect of internal moving parts on projectile flight dynamics and control. Early work focused on instabilities caused by moving parts, while more recent work has investigated the use of internal moving parts as a control mechanism. Soper [2] and Murphy [3] analytically evaluated the stability of a spinning projectile that contains a cylindrical mass fitted loosely into a cylindrical cavity. Later, D'Amico [4] performed a detailed series of experiments where a projectile with a loose internal part was driven by the rotor of a freely gimbaled gyroscope. Hodapp [5] expanded the work of Soper [2] and Murphy [3] by considering a projectile configuration with a partially restrained internal member with a mass centre offset. More recently, Petsopoulos *et al.* [6] considered employment of a moving mass inside a re-entry vehicle to create a means for roll control. Robinett *et al.* [7] used internally moving masses in a plane normal to the axis of

*Corresponding author: School of Aerospace Engineering, Georgia Institute of Technology, Atlanta, Georgia 30332, USA.
email: mark.costello@ae.gatech.edu*

symmetry of ballistic rockets to achieve control, while Menon et al. [8] considered both exoatmospheric and endoatmospheric interception scenarios using three orthogonal internal translating masses as the control mechanism. Frost and Costello [9, 10] investigated the ability of an internal rotating mass unbalance to actively control both fin- and spin-stabilized projectiles. Most recently, Rogers and Costello [11] examined the control authority of a projectile equipped with an internal laterally translating mass.

This article considers a projectile configuration whereby stability margin of the round is altered during flight by moving an internal mass in a controlled fashion along the projectile's line of symmetry. This mass movement occurs at some point after launch. The system has high initial static stability and proves to be less vulnerable to launch disturbances. After mass movement, stability margin decreases and the projectile becomes more responsive to control input. An example case shows that the variable stability mechanism can result in decreased throw-off error, more divert capability, and less average force required to achieve a given circular error probable (CEP). A range of trade studies are reported varying the internal mass ratio, error budget, and maximum control force. Note that the main focus of this article is not to study the effects of static margin on launch perturbations or control authority, areas that have been thoroughly explored in the past, but rather to examine the impact of a mechanism for active static margin control through mass centre modification on overall system performance. This impact is measured explicitly by the projectile's ability to hit the target and the control force required to do so, given reasonable launch perturbations and limited control authority. The system is developed specifically for smart munitions, which routinely suffer from a lack of required control authority, rather than missiles, which often do not exhibit the same control authority limitations.

## 2 VARIABLE STABILITY PROJECTILE DYNAMIC MODEL

The system consists of two major components, namely a main projectile body and an internal translating mass. The main projectile body is largely a typical projectile with the exception of an internal cavity that hosts an internal mass. The internal mass is free to translate within the main projectile cavity. An actuator inside the projectile exerts a force on the internal mass as well as the main projectile to move the mass inside the cavity to a desired location. A schematic of the variable stability projectile is shown in Fig. 1. Note that the cavity is aligned with the body centre-line (axis of symmetry).

Two reference frames are used in development of the equations of motion for the system, namely the inertial and projectile reference frames. The two frames are linked by the following orthonormal transformation matrix

$$\begin{Bmatrix} I_P \\ J_P \\ K_P \end{Bmatrix} = \begin{bmatrix} c_\theta c_\psi & c_\theta s_\psi & -s_\theta \\ s_\phi s_\theta c_\psi - c_\phi s_\psi & s_\phi s_\theta s_\psi + c_\phi c_\psi & s_\phi c_\theta \\ c_\phi s_\theta c_\psi + s_\phi s_\psi & c_\phi s_\theta s_\psi - s_\phi c_\psi & c_\phi c_\theta \end{bmatrix} \begin{Bmatrix} I_I \\ J_I \\ K_I \end{Bmatrix}$$

$$= [\mathbf{T}_{IP}] \begin{Bmatrix} I_I \\ J_I \\ K_I \end{Bmatrix} \tag{1}$$

The cavity containing the internal translating mass is fixed and extends along the projectile's axis of symmetry, in this case the $I_P$ axis. All equations use the following shorthand notation for trigonometric sine, cosine, and tangent functions: $s_\alpha = \sin\alpha$, $c_\alpha = \cos\alpha$, and $t_\alpha = \tan\alpha$.

Throughout the development of the equations of motion, several different position vectors are used. The nomenclature for position vectors is such that $r_{\alpha \to \beta}$ is defined as the position vector from point $\alpha$ to point $\beta$. The position vector of the mass centre of the two-body system with respect to a ground fixed reference frame is written as

$$r_{O \to C} = x I_I + y J_I + z K_I \tag{2}$$

while the position of the internal translating mass with respect to the projectile reference frame is

$$r_{C \to T} = (x_T + s) I_P \tag{3}$$

The mathematical model describing the motion of the internal translating mass projectile allows for four
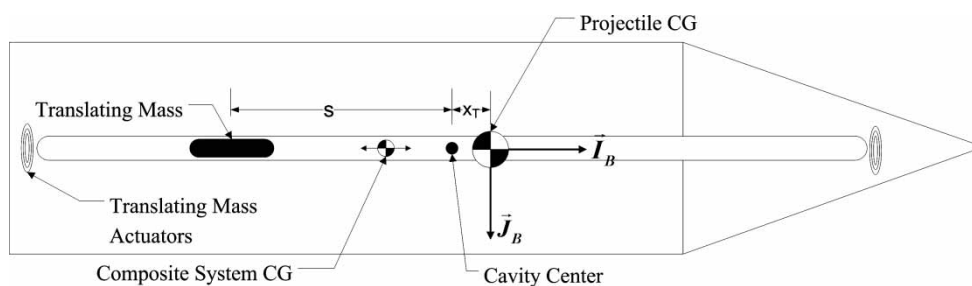


Fig. 1 Schematic of the variable stability projectile configuration

translational and three rotational rigid body degrees of freedom. The translational degrees of freedom are the three components of the composite body mass centre position vector $(x, y, z)$ and the position of the internal translating mass with respect to the projectile body $(s)$. The rotation degrees of freedom are the Euler roll, pitch, and yaw angles $(\phi, \theta, \psi)$ mentioned above.

The vector component operator used below outputs a column vector comprised of the components of an input vector in a given frame. For example, if the position vector from $\alpha$ to $\beta$ is expressed in reference frame $A$ as $\boldsymbol{r}_{\alpha \to \beta} = \Delta x_{\alpha\beta} \overrightarrow{I}_A + \Delta y_{\alpha\beta} \overrightarrow{J}_A + \Delta z_{\alpha\beta} \overrightarrow{K}_A$, then the vector component operator acting on this vector yields

$$\mathbb{C}_A(\boldsymbol{r}_{\alpha \to \beta}) = \begin{Bmatrix} \Delta x_{\alpha\beta} \\ \Delta y_{\alpha\beta} \\ \Delta z_{\alpha\beta} \end{Bmatrix} \tag{4}$$

Notice that the reference frame is denoted by the subscript on the operator. In a similar way, the cross-product operator outputs a skew symmetric matrix using the components of an input vector in the reference frame denoted in the subscript

$$\mathbb{S}_A(\boldsymbol{r}_{\alpha \to \beta}) = \begin{bmatrix} 0 & -\Delta z_{\alpha\beta} & \Delta y_{\alpha\beta} \\ \Delta z_{\alpha\beta} & 0 & -\Delta x_{\alpha\beta} \\ -\Delta y_{\alpha\beta} & \Delta x_{\alpha\beta} & 0 \end{bmatrix} \tag{5}$$

## 2.1 Kinematics

The velocity of the composite body mass centre can be described in the inertial frame or the projectile reference frame

$$\boldsymbol{v}_{C/I} = \dot{x}\boldsymbol{I}_I + \dot{y}\boldsymbol{J}_I + \dot{z}\boldsymbol{K}_I = u\boldsymbol{I}_P + v\boldsymbol{J}_P + w\boldsymbol{K}_P \tag{6}$$

The translational kinematic differential equations relate these two representations of the mass centre velocity components

$$\begin{Bmatrix} \dot{x} \\ \dot{y} \\ \dot{z} \end{Bmatrix} = \begin{bmatrix} c_\theta c_\psi & s_\phi s_\theta c_\psi - c_\phi s_\psi & c_\phi s_\theta c_\psi + s_\phi s_\psi \\ c_\theta s_\psi & s_\phi s_\theta s_\psi + c_\phi c_\psi & c_\phi s_\theta s_\psi - s_\phi c_\psi \\ -s_\theta & s_\phi c_\theta & c_\phi c_\theta \end{bmatrix} \begin{Bmatrix} u \\ v \\ w \end{Bmatrix}$$

$$= [\mathbf{T}_{IP}]^T \begin{Bmatrix} u \\ v \\ w \end{Bmatrix} \tag{7}$$

The angular velocity of the projectile with respect to the inertial reference frame can be written in terms of appropriate Euler angle time derivatives or in terms of projectile frame angular velocity components

$$\boldsymbol{\omega}_{P/I} = \dot{\phi}\boldsymbol{I}_P + \dot{\theta}\boldsymbol{J}_N + \dot{\psi}\boldsymbol{K}_I = p\boldsymbol{I}_P + q\boldsymbol{J}_P + r\boldsymbol{K}_P \tag{8}$$

The kinematic relationship between time derivatives of the Euler angles and projectile reference frame

angular velocity components represents the rotational kinematic differential equations

$$\begin{Bmatrix} \dot{\phi} \\ \dot{\theta} \\ \dot{\psi} \end{Bmatrix} = \begin{bmatrix} 1 & s_\phi t_\theta & c_\phi t_\theta \\ 0 & c_\phi & -s_\phi \\ 0 & s_\phi/c_\theta & c_\phi/c_\theta \end{bmatrix} \begin{Bmatrix} p \\ q \\ r \end{Bmatrix} \tag{9}$$

The final kinematic differential equation is the trivial relationship

$$\dot{s} = v_S \tag{10}$$

## 2.2 Dynamics

The reader is referred to reference [11] for a complete derivation of the dynamic equations for a projectile equipped with an internal translating mass. The variable stability projectile dynamic equations used here are formed by substituting $\psi_T = \theta_T = 0$ into the dynamic equations given in reference [11], representing internal translating mass movement along the projectile centreline. Three translational dynamic equations are derived through force balancing. The sum of all external forces on the system must equal the mass of the system multiplied by the acceleration of the system mass centre, and thus three translational dynamic equations are given by

$$\begin{Bmatrix} \dot{u} \\ \dot{v} \\ \dot{w} \end{Bmatrix} = \begin{Bmatrix} \dfrac{X}{m} \\ \dfrac{Y}{m} \\ \dfrac{Z}{m} \end{Bmatrix} - \begin{bmatrix} 0 & -r & q \\ r & 0 & -p \\ -q & p & 0 \end{bmatrix} \begin{Bmatrix} u \\ v \\ w \end{Bmatrix} \tag{11}$$

Additionally, another translational dynamic equation is found by writing a force balance equation on the translating mass and applying the well-known two points on a rigid body formula for acceleration. This fourth translational dynamic equation is given by

$$[A_{S1} \quad A_{S2} \quad A_{S3}] \begin{Bmatrix} \dot{u} \\ \dot{v} \\ \dot{w} \\ \ddot{s} \\ \dot{p} \\ \dot{q} \\ \dot{r} \end{Bmatrix} = \{B_S\} \tag{12}$$

where

$$A_{S1} = m_T[1, 0, 0] \tag{13}$$

$$A_{S2} = \frac{m_P m_T}{m} \tag{14}$$

$$A_{S3} = -\frac{m_P m_T}{m}[1, 0, 0]\mathbb{S}_P(\boldsymbol{r}_{P \to T}) \tag{15}$$

$$B_S = f_{input} - c_V \dot{s} - m_T g s_\theta$$
$$- m_T[1, 0, 0]\mathbb{S}_P(\boldsymbol{\omega}_{P/I})\mathbb{C}_P(\boldsymbol{v}_{C/I})$$
$$- \frac{m_P m_T}{m}[1, 0, 0]\mathbb{S}_P(\boldsymbol{\omega}_{P/I})\mathbb{S}_P(\boldsymbol{\omega}_{P/I})\mathbb{C}_P(\boldsymbol{r}_{P \to T}) \quad (16)$$

The rotation kinetic differential equations are obtained by equating the $I$ frame time rate of change of the system angular momentum about the system mass centre to the total applied external moments to the system about the system mass centre

$$\frac{^I d\boldsymbol{H}_{P/I}^P}{dt} + \frac{^I d\boldsymbol{H}_{T/I}^T}{dt} + m_P \boldsymbol{r}_{C \to P} \times \boldsymbol{a}_{P/I} + m_T \boldsymbol{r}_{C \to T} \times \boldsymbol{a}_{T/I}$$
$$= \boldsymbol{M}^C \quad (17)$$

Expressed in the projectile reference frame, the components of the rotation kinetic differential equations are

$$\mathbf{A}_{RR} \begin{Bmatrix} \dot{p} \\ \dot{q} \\ \dot{r} \end{Bmatrix} + A_{RS}\{\ddot{s}\} = \{\boldsymbol{B}_R\} \quad (18)$$

where

$$\mathbf{A}_{RR} = \mathbf{I}_P + \mathbf{I}_T - \frac{m_T}{m_P}m\mathbb{S}_P(\boldsymbol{r}_{C \to T})\mathbb{S}_P(\boldsymbol{r}_{C \to T}) \quad (19)$$

$$A_{RS} = m_T\mathbb{S}_P(\boldsymbol{r}_{C \to T}) \quad (20)$$

$$\boldsymbol{B}_R = \begin{Bmatrix} M_X \\ M_Y \\ M_Z \end{Bmatrix} - \mathbb{S}_P(\vec{\boldsymbol{\omega}}_{P/I})$$
$$\times \left(\mathbf{I}_P + \mathbf{I}_T - \frac{m_T}{m_P}m\mathbb{S}_P(\boldsymbol{r}_{C \to T})\mathbb{S}_P(\boldsymbol{r}_{C \to T})\right)\mathbb{C}_P(\boldsymbol{\omega}_{P/I})$$
$$- 2m_T\mathbb{S}_P(\boldsymbol{r}_{C \to T})\mathbb{S}_P(\boldsymbol{\omega}_{P/I}) \begin{Bmatrix} \dot{s} \\ 0 \\ 0 \end{Bmatrix} \quad (21)$$

The dynamic equations of motion for the internal translating mass projectile are collectively given by equations (7), (9) to (12), and (18). With a known set of initial conditions for the projectile, these 14 scalar equations are numerically integrated forward in time using a fourth-order Runge–Kutta algorithm to obtain a single trajectory. The model used for all simulations below has been validated against an industry-standard six-degree-of-freedom model to verify the accuracy of results. Details of this validation are provided in reference [11].

## 2.3 Projectile applied forces and moments

The standard aerodynamic expansion employed for projectile flight dynamic simulation is used here. A description of the weight force and body aerodynamic forces and moments are provided in reference [11].

## 2.4 Description of translating mass controller

The control force exerted on the internal translating mass is generated by a feedback linearization controller [12] that assumes full-state feedback. The equation used to compute the control force is

$$f_{input} = \frac{m_P m_T}{m}[\ddot{s}_{command} - k_1(\dot{s} - \dot{s}_{command})$$
$$- k_0(s - s_{command})] - b + A_{S1} \begin{Bmatrix} \dot{u} \\ \dot{v} \\ \dot{w} \end{Bmatrix} + A_{S3} \begin{Bmatrix} \dot{p} \\ \dot{q} \\ \dot{r} \end{Bmatrix}$$
$$(22)$$

where $b$ is given by

$$b = -c_V \dot{s} - m_T g s_\theta - m_T[1, 0, 0]\mathbb{S}(\boldsymbol{\omega}_{P/I})\mathbb{C}(\boldsymbol{v}_{C/I})$$
$$- \frac{m_P m_T}{m}[1, 0, 0]\mathbb{S}(\boldsymbol{\omega}_{P/I})\mathbb{S}(\boldsymbol{\omega}_{P/I})\mathbb{C}(\boldsymbol{r}_{P \to T}) \quad (23)$$

and $A_{S1}$ and $A_{S3}$ are given by equations (13) and (15), respectively. For all cases below, values of $k_1 = 30$ and $k_0 = 500$ were used.

## 2.5 Description of flight control system

In order to perform a general analysis, it is assumed that an unspecified control mechanism is capable of exerting a lateral force on the projectile at some point on the body subsequently yielding an associated control moment. The control force is limited to a specific value. The control law used is proportional navigation guidance (PNG) [13], a standard guidance law used in many smart weapon designs. Proportional navigation seeks to force the line of sight angle between the projectile and the target to be constant. Therefore, the acceleration command generated by PNG can be written as

$$\vec{A}_C = N_C \vec{V}_C \dot{\lambda} \quad (24)$$

where $\vec{A}_C$ is the acceleration command, $N_C$ is the PNG gain, $\vec{V}_C$ is the missile-target closing velocity, and $\lambda$ is the line-of-sight angle. Let the $L$ frame denote a reference frame with unit vector $\boldsymbol{I}_L$ aligned with the line-of-sight between the projectile and the target, $\boldsymbol{J}_L$ lying in the plane formed by $\boldsymbol{I}_P$ and $\boldsymbol{J}_P$, and $\boldsymbol{K}_L$ completing the right-handed triad. Then equation (24) can be expressed as

$$\boldsymbol{A}_C = -N_C \boldsymbol{v}_{C/I} \times \boldsymbol{\omega}_{L/I} \quad (25)$$

Also, noting that

$$\boldsymbol{\omega}_{L/I} = \frac{-\boldsymbol{r}_{C \to X} \times \boldsymbol{v}_{C/I}}{|\boldsymbol{r}_{C \to X}|^2} \quad (26)$$

where $\boldsymbol{r}_{C\to X}$ denotes the distance vector from the system mass centre to the impact point, the PNG-generated acceleration command can finally be written as

$$\boldsymbol{A}_C = \frac{N_C}{|\boldsymbol{r}_{C\to X}|^2}\boldsymbol{v}_{C/I} \times (\boldsymbol{r}_{C\to X} \times \boldsymbol{v}_{C/I}) \qquad (27)$$

All cases below use a PNG gain of 3.0.

## 3 RESULTS

The example projectile used to examine the effectiveness of the variable stability mechanism is a representative indirect fire, fin-stabilized projectile with a reference diameter of 105 mm and approximate length of 0.579 m. This projectile's mass, roll inertia, and pitch inertia are 17.606 kg, 0.0377 kg m$^2$, and 0.8530 kg m$^2$, respectively. For all variable stability cases, the cavity containing the internal mass is centred along the projectile $\boldsymbol{I}_P$ axis and has a length approximately equal to the length of the projectile.

Several case studies are examined first using rounds not equipped with the variable stability mechanism in order to understand the effect of centre of gravity (CG) position on uncontrolled CEP for a nominal munition, as well as to determine the effect of CG position on required maximum control force. Once these relationships are determined, the variable stability mechanism is introduced in a similar framework to show its ability to both decrease 'throw-off' errors and to minimize control forces required to hit a given target. Throw-off errors, otherwise known as aerodynamic jump, are trajectory alterations caused by non-zero crossing velocities and roll rates at launch, and have been shown to contribute significantly to dispersion. In cases where a CEP is generated, three error budgets for initial conditions are used, referred to as 'low error', 'medium error', and 'high error'. The standard deviations for each of these error budgets, as well as the bias used in generating them, are given in Table 1. Note that '$\sigma$' denotes standard deviation and

wind azimuth is a uniform random variable between 0 and $2\pi$.

The first study examines the effect of CG position on uncontrolled CEP of the example projectile. Two hundred Monte Carlo cases were run for each error budget at each CG location to generate the uncontrolled CEP. Figure 2 shows that, as expected, CEP grows significantly as the CG moves aft (and the projectile becomes less statically stable). This is mainly due to initial throw-off error experienced by the projectile during launch. Analysis of trajectory data from these dispersion simulations revealed that rounds with low stability experience significantly higher angles of attack. At the same time, projectiles with lower stability margin (a CG further aft) respond more to control inputs than higher stability rounds. Figure 3 shows that the same amount of control force generates more cross-range in a less stable round than a more stable round. The same case was run with zero-error initial conditions for the same array of CG locations as in the first study above. Throughout the trajectory, a constant control force in the $\boldsymbol{J}_I$ direction was exerted on the projectile
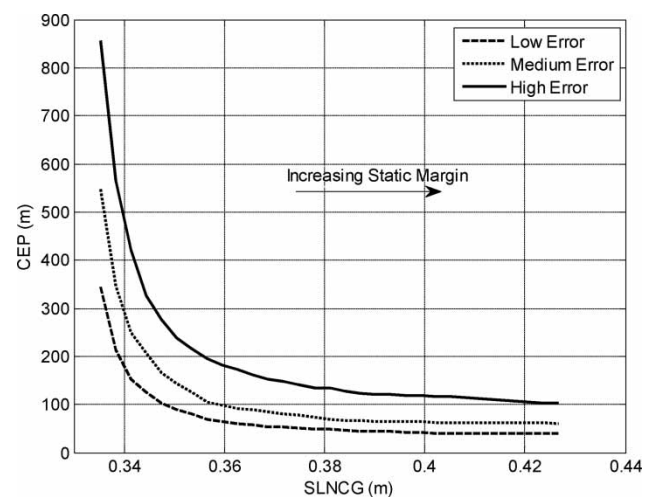


**Fig. 2** Uncontrolled CEP versus stationline CG position

**Table 1** Error budget parameters

| States | Example indirect fire | | | | Example direct fire | |
| | Bias | $\sigma$ – low | $\sigma$ – medium | $\sigma$ – high | Bias | $\sigma$ |
|---|---|---|---|---|---|---|
| $x$ (m) | 0.0 | 0.0 | 0.0 | 0.0 | 0.0 | 0.0 |
| $y$ (m) | 0.0 | 0.0 | 0.0 | 0.0 | 0.0 | 0.0 |
| $z$ (m) | 0.0 | 0.0 | 0.0 | 0.0 | 0.0 | 0.0 |
| $\Phi$ (rad) | 0.0 | 0.0 | 0.0 | 0.0 | 0.0 | 0.0 |
| $\theta$ (rad) | 0.05 | 0.000 15 | 0.000 31 | 0.0005 | 0.0 | 0.000 31 |
| $\psi$ (rad) | 0.0 | 0.000 08 | 0.000 16 | 0.000 25 | 0.0 | 0.000 16 |
| $u$ (m/s) | 860.8 | 2.44 | 3.20 | 4.57 | 1731.0 | 6.10 |
| $v$ (m/s) | 0.0 | 0.55 | 0.91 | 1.52 | 0.0 | 1.52 |
| $w$ (m/s) | 0.0 | 0.55 | 0.91 | 1.52 | 0.0 | 1.52 |
| $p$ (rad/s) | 5.0 | 0.8 | 1.5 | 2.0 | 0.0 | 1.5 |
| $q$ (rad/s) | 0.0 | 0.6 | 1.0 | 1.7 | 0.0 | 1.0 |
| $r$ (rad/s) | 0.0 | 0.6 | 1.0 | 1.7 | 0.0 | 1.0 |
| Wind (m/s) | 0.0 | 3.66 | 5.58 | 6.40 | 0.0 | 5.58 |

and the cross-range of the impact point was recorded. Figures 2 and 3 demonstrate that there exists a fundamental trade-off in projectile design between a highly stable round, which requires greater control force, and a less stable round, which is more susceptible to initial throw-off error. These factors are characterized by the 'controllability' effect, which refers to how responsive a round is to control force, and the 'throw-off' effect, which refers to how vulnerable a round is to disturbances. A Monte Carlo simulation using the controlled example round examines how these two effects interact and ultimately shows that there is a CG location that optimizes these two effects to produce a minimum required control force.

As described above, a PNG control law was used on the example munition to guide the projectile to the impact point $x = 4938$ m, $y = -0.91$ m, and $z = 0.0$ m. A set of 200 Monte Carlo runs were completed for each CG location to generate a controlled CEP. A time history of control forces for each trajectory was collected, and then all 200 time histories were averaged to produce a single 'average force' value for each CG location. Control forces, applied 15.24 cm forward of the projectile mass centre, were limited to 266.9 N in both the $J_P$ and $K_P$ directions, and sensor errors were not included. The controller was activated for 4 s into each trajectory. Figure 4 shows the controlled CEP for each CG location, while Fig. 5 shows the average force required for each CG location as described above. Figure 4 shows that, except for marginally stable rounds that proved either too difficult to control or suffered from uncorrectable launch errors, the controller is quite effective at hitting the target. Interestingly, Fig. 5 shows there is actually an 'optimum' CG location where control force required is at a minimum. Rounds with CG positions forward of this require more effort by the controller to manoeuvre the round, while
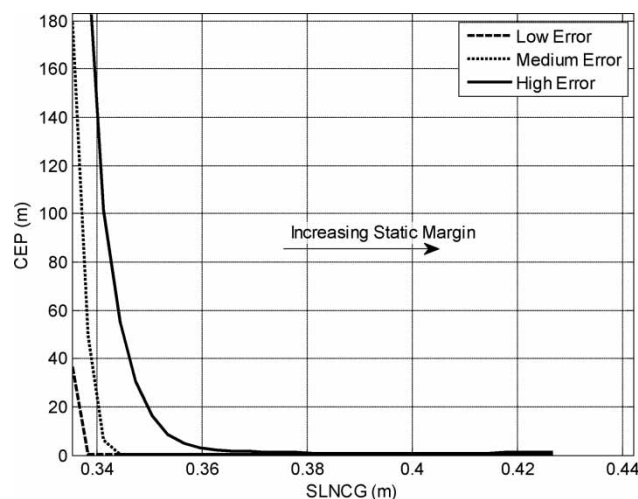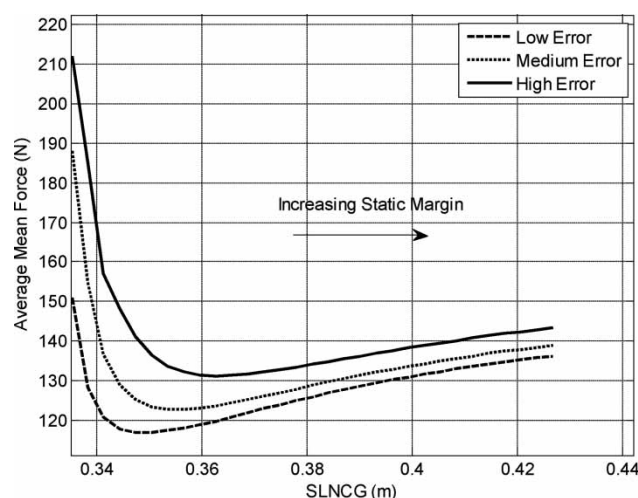


**Fig. 4** Controlled CEP versus stationline CG position



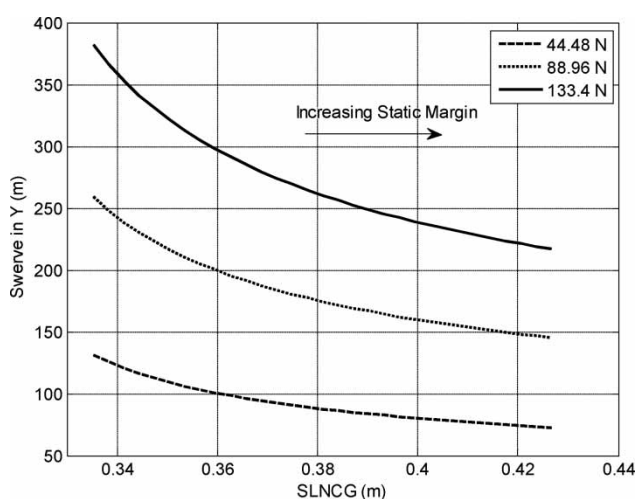**Fig. 5** Average force required versus stationline CG position

rounds with CG position aft of this suffer from substantial initial error and thus require more force to correct the trajectory. In this way, the 'controllability' and 'throw-off' effects play off one another to create an optimum CG location. These results were also verified for an example of direct fire case for a fin-stablilized projectile. It is interesting to note that results from the indirect and direct fire case demonstrated that the optimum CG location varies as a function of error budget and range to target.

Incorporating the variable stability mechanism into the example round, it can be shown that an increase in the projectile's stability for only a fraction of second beyond launch is sufficient to mitigate most throw-off error. Once initial perturbations of the round vanish, the remainder of the flight can be conducted with reduced stability with little effect on uncontrolled CEP. For comparison purposes, two projectiles were considered. The first, referred to as the 'reduced stability'



**Fig. 3** Cross-range of impact point versus stationline CG position for varying constant control forces

round, is the example munition without the variable stability mechanism and a CG farther aft than nominal. The other, the 'variable stability' round, is the example munition with the variable stability mechanism incorporated. Uncontrolled CEPs were generated for both rounds using the 'medium error' set of initial conditions. For all variable stability cases below, the mass was placed initially as far forward as possible, and then translated aft approximately 0.3 s into the trajectory. The experiment was designed such that with the mass in the aft position the variable stability round had identical stability characteristics to the reduced stability round. Figure 6 shows the static margin, defined as the distance between the total centre of pressure and the mass centre, of both the reduced and variable stability rounds for one of the above simulations. Note that the static margin of the variable stability round is initially higher, and after mass translation the stability of both projectiles is identical. Figure 7 shows the position of the translating mass with respect to the projectile throughout the variable stability trajectory in order to demonstrate how mass movement occurs in flight.

Table 2 summarizes CEP results for both cases, run for two different translating mass percentages. Notice that, although the majority of the trajectory is flown at identical stability margins, the variable stability round has significantly smaller CEP than the reduced stability round. This is due to its higher initial stability, which allows initial errors (the primary cause of dispersion) to be mitigated much more effectively.

With the knowledge that an optimal CG location exists and that the use of the internal moving mass can substantially reduce throw-off error as shown in Table 2, the variable stability mechanism can be implemented in a controlled round to increase control authority. In a round with a given available control force, this is equivalent to greater control authority.
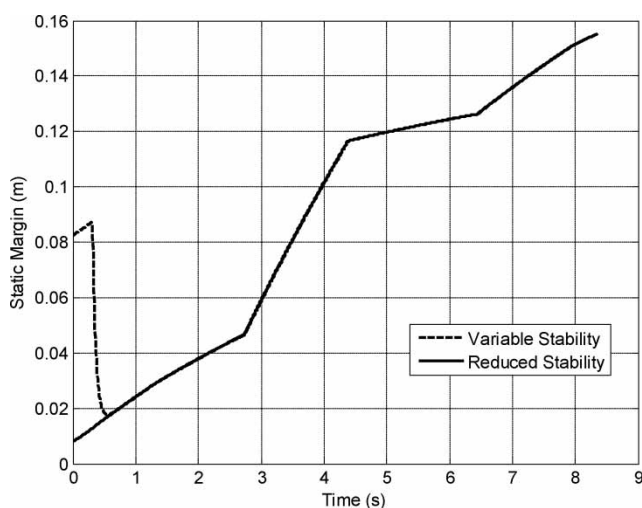


**Fig. 6** Stability margin versus time for variable and reduced stability rounds for a single simulation
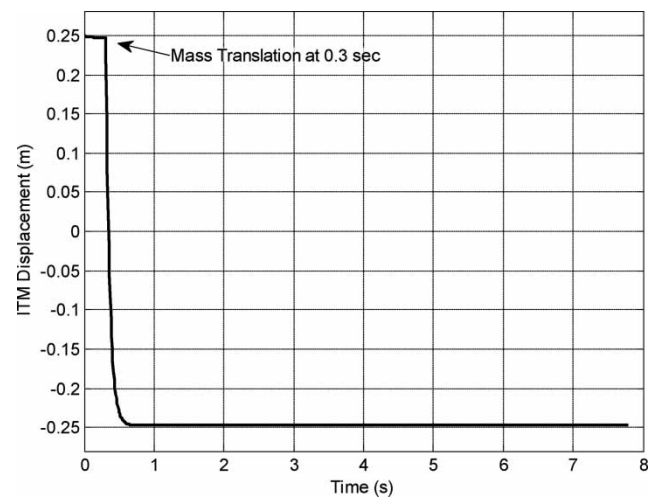


**Fig. 7** ITM displacement versus time for example variable stability trajectory

**Table 2** CEP for reduced and variable stability rounds

| Case | Internal mass percentage | Initial CG stationline (m) | Final CG stationline (m) | Impact point range (m) | CEP (m) |
|---|---|---|---|---|---|
| 1 – reduced | N/A | 0.3667 | 0.3667 | 4754 | 89.13 |
| 1 – variable | 5 | 0.3978 | 0.3667 | 4757 | 55.55 |
| 2 – reduced | N/A | 0.3417 | 0.3417 | 4913 | 93.32 |
| 2 – variable | 13 | 0.4164 | 0.3417 | 4917 | 54.39 |

To demonstrate this, the variable stability mechanism is implemented in the example projectile along with the PNG guidance system with control force limits of 111.2 N in both the $J_P$ and $K_P$ directions. The cavity is approximately 12 per cent of the total projectile volume and the translating mass is 8 per cent of the total projectile mass. Two rigid projectiles, equivalent in mass to the variable stability round, are also used for comparison purposes. The first has a CG location equal to the variable stability round's CG location before mass translation, while the second has a CG location equal to that of the variable stability round after mass translation. The rigid round with the forward CG location is called 'highly stable', while the round with the aft CG location is called 'reduced stability'. The projectile equipped with the variable stability mechanism is referred to as 'variable stability'.

To compare the highly stable, the reduced stability, and the variable stability rounds, the target was placed at $x = 4755$ m, $y = -76.2$ m, and $z = 0.0$ m. The controller was turned on 4.0 s into the flight, representing a reasonable amount of time for sensor systems and other electronics to be powered on and initialized after launch. Randomly generated initial conditions were used: $x = 0.0$ m, $y = 0.0$ m, $z = 0.0$ m, $\varphi = 0.0$ rad, $\theta = 0.0499$ rad, $\psi = 0.0$ rad, $u = 860.91$ m/s, $v = 1.658$ m/s, $w = 1.089$ m/s,

$p = 5.26 \, \text{rad/s}, \; q = -0.18 \, \text{rad/s}, \; r = 0.72 \, \text{rad/s}, \;$ wind magnitude $= 3.29 \, \text{m/s}$, and wind azimuth $= 5.12 \, \text{rad}$. Figures 8 to 10 show the trajectories, while Fig. 11 shows time histories of the magnitude of the control forces for all three rounds. The reduced stability round misses the target by almost 200 m because of the large throw-off error, as can be clearly seen in Fig. 9. The highly stable round misses the target by approximately 20 m, since there is insufficient control authority with the given force limit to achieve the commanded cross-range. However, the variable stability projectile hits the target nearly exactly because of its small initial throw-off and its relatively large control authority. Figure 11 confirms this, as the controller for both the highly stable and the reduced stability rounds is saturated through the entire trajectory, while the controller for the variable stability round is out of saturation for a significant portion of the flight. The term 'saturation' is used here to mean that the controller is using the
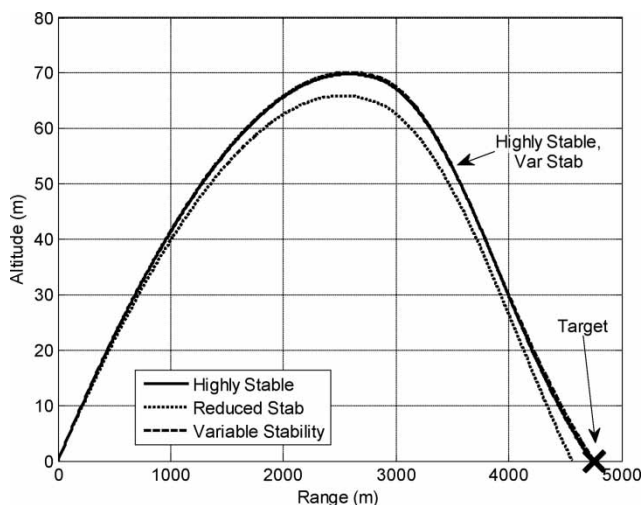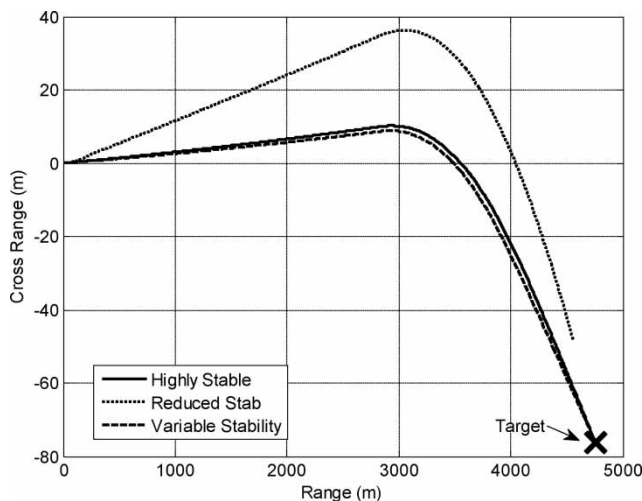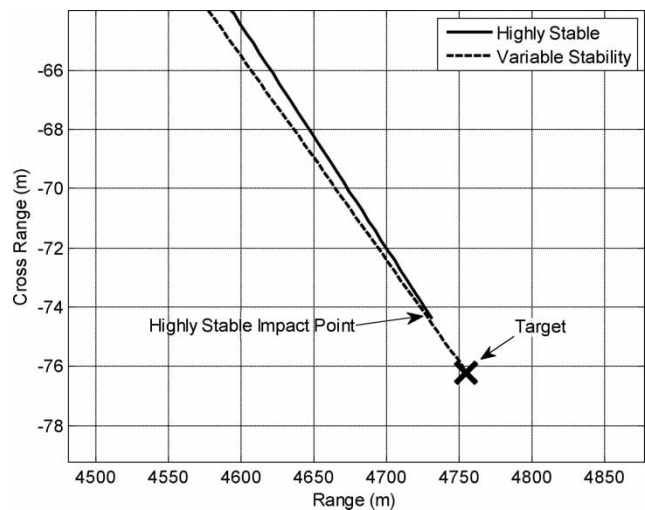


**Fig. 10** Zoom view of cross-range versus range near target
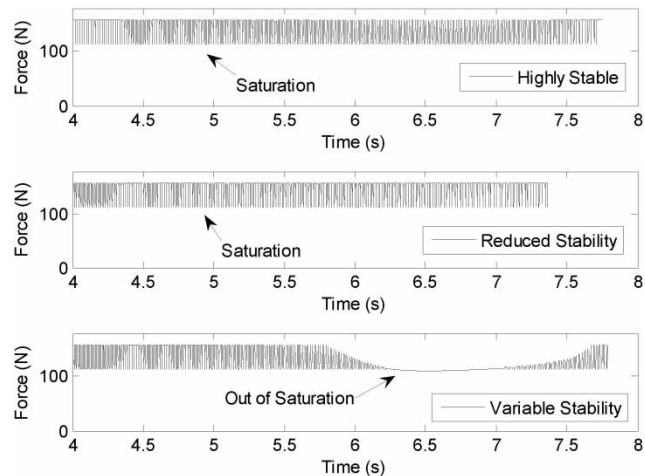


**Fig. 8** Altitude versus range



**Fig. 11** Control force magnitude versus time

maximum control force available to it, which oscillates between the maximum available in one direction (111.2 N) and the magnitude of the maximum available in both directions (157.3 N) as the projectile rolls. Therefore, as seen in Fig. 11, for the variable stability case the controller does not require all available control for the variable stability case, while for the other cases it does. Furthermore, the average force required is 140.6 N for the highly stable round, 149.9 N for the reduced stability round, and 129.0 N for the variable stability round. Note that the average force required for the projectile equipped with the variable stability mechanism is almost 10 per cent less than that required for the highly stable round, and almost 17 per cent less than that required for the reduced stability round, neither of which was able to achieve the desired divert distance.

The benefit of the variable stability mechanism can be further explored by comparing dispersion of the



**Fig. 9** Cross-range versus range

highly stable, reduced stability, and the variable stability rounds. Figures 12 to 16 show the controlled CEP as a function of maximum manoeuvre control force for various internal mass sizes. Table 3 shows the change in mass centre stationline affected by mass translation in the variable stability round. In all cases, the mass centre stationline after mass translation ('aft CG stationline') is the same, since an attempt was made to keep a static margin of at least 2/10 calibre throughout the entire flight. The CEPs were generated using the 'high error' budget with the example projectile, and control force was exerted 4.0 s after launch. The 95 per cent mass case (meaning that 95 per cent of the system mass consists of the internal translating mass) may be realized as a hollow aeroshell within which nearly the entire mass of the projectile may be translated. Also, note that as mass percentage is increased, there is a corresponding change in total
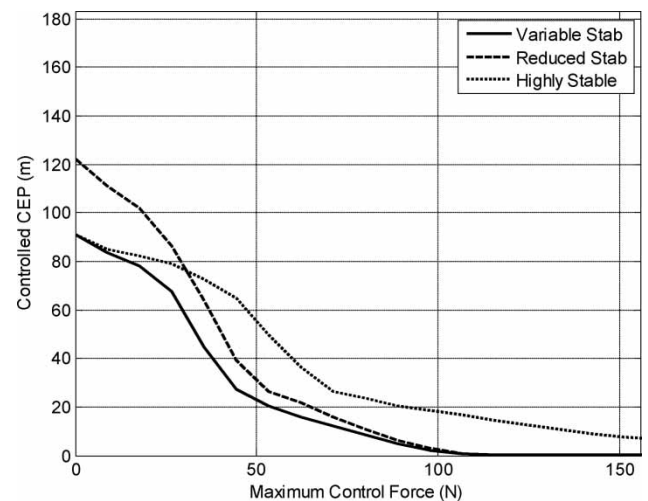


**Fig. 14** Controlled CEP versus maximum allowable control force, 65 per cent mass
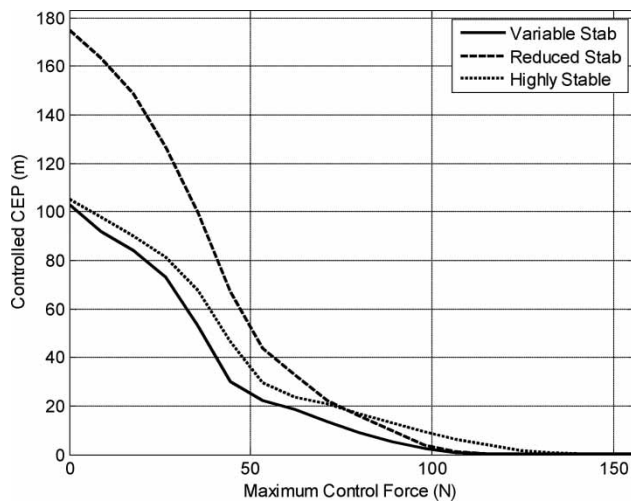


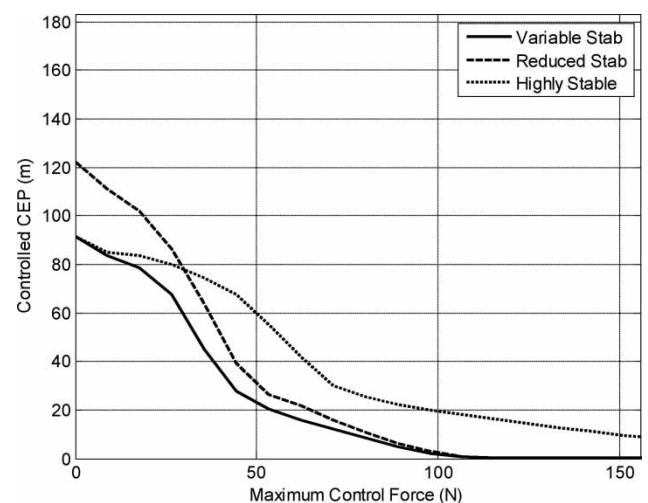**Fig. 12** Controlled CEP versus maximum allowable control force, 10 per cent mass



**Fig. 15** Controlled CEP versus maximum allowable control force, 95 per cent mass
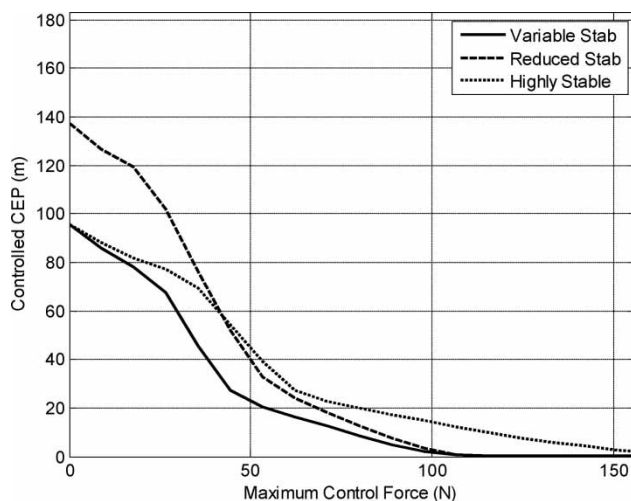


**Fig. 13** Controlled CEP versus maximum allowable control force, 30 per cent mass
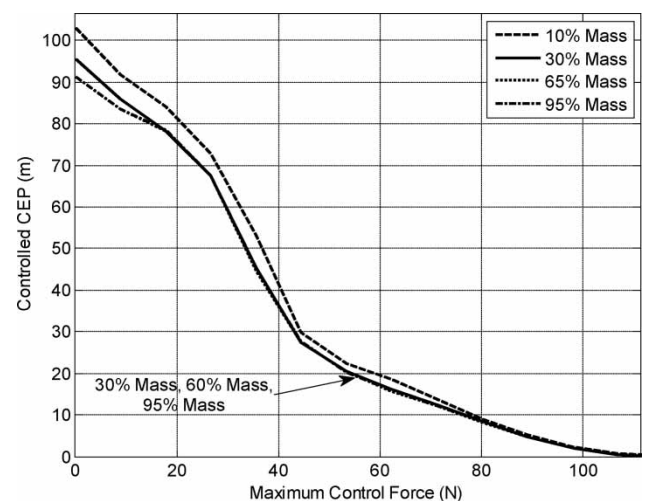


**Fig. 16** Controlled CEP versus maximum allowable control force, variable stability rounds

pitch moment of inertia. Moments of inertia of the rigid projectiles were therefore changed in each different mass percentage case in order to match the variable stability mass properties with the rigid projectile mass properties. In Figs 12 to 15, the controlled CEP at zero maximum manoeuvre control force (equivalent to uncontrolled CEP, since no force can be exerted by the controller) for the highly stable and variable stability rounds are nearly identical, demonstrating that both rounds exhibit the same response to initial perturbations. This further proves that mass translation after initial perturbations dissipate has little effect on the trajectory if no control force is exerted.

As Figs 12 to 15 show, the variable stability mechanism shows better overall performance in reducing CEP for a given maximum force level than equivalent rigid rounds. The reduced stability round shows less dispersion as mass percentage increases because of the corresponding decrease in pitch moment of inertia (reducing the effect of initial perturbations). The highly stable round actually shows more dispersion as mass percentage increases, even though the round is more stable throughout the flight. This is because, as described above and in Fig. 5, the disadvantage of reduced control authority outweighs the benefit of increased stability at these mass centre locations.

Figure 16 shows the same variable stability CEP curves as in Figs 12 to 15 for each mass percentage and establishes an important design benchmark for implementation of the variable stability mechanism. It is clear that at some mass percentage between 10 and 30 per cent, further increases in mass percentage produce little to no benefit in reducing dispersion for a given maximum manoeuvre control force. First, it should be noted that all cases had the same mass centre position after mass translation as described above, and therefore exhibited the same control authority during controlled portions of flight. The cases differed only in their initial mass centre position, with the 95 per cent case being the most stable at launch and the 10 per cent case being the least stable. However, at some point further increases in projectile stability have little effect on reducing launch perturbations, and therefore little difference is seen between the 30, 65, and 95 per cent cases. Thus in this case, a mass percentage of between 20 and 30 per cent would probably be sufficient to provide the maximum benefit that the variable

stability mechanism has to offer in terms of reducing dispersion and increasing control effectiveness.

Figures 17 and 18, based on the results above, demonstrate a further trade-off when considering mass size. Figure 17 shows that for low maximum force levels (0–45 N) the percentage decrease in CEP resulting from the variable stability mechanism when compared to the highly stable round is quite steep with respect to force level, and there is a local maximum for all mass sizes around 45–67 N. Also, note that the 95 per cent mass case shows the most improvement in percentage decrease in CEP compared to the highly stable round. However, Fig. 18 demonstrates that the variable stability mechanism shows relatively constant percentage decreases in CEP over all force levels compared to the reduced stability round for each mass
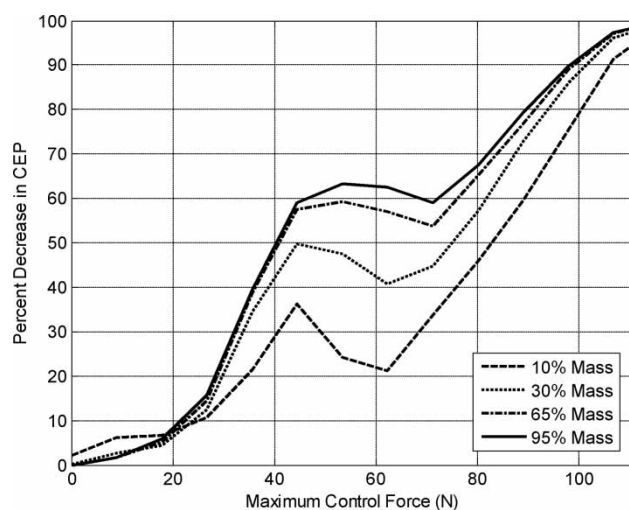


**Fig. 17**  Percentage decrease in CEP of variable stability projectile compared to highly stable projectile
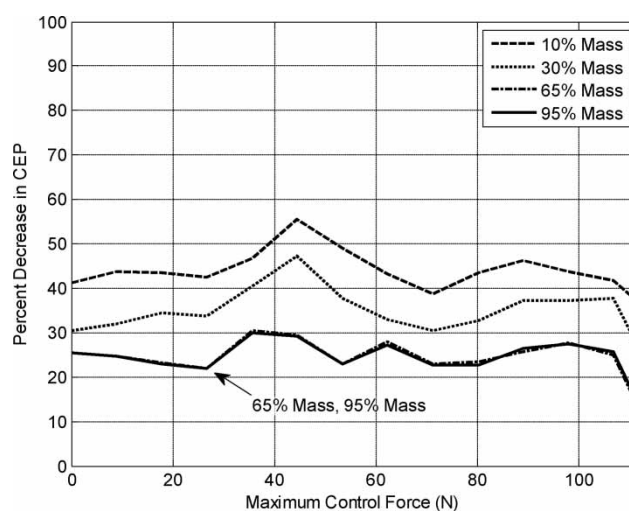


**Fig. 18**  Percentage decrease in CEP of variable stability projectile compared to reduced stability projectile

**Table 3**  Mass centre position for various translating mass percentages

| Mass percentage | Forward CG stationline (m) | Aft CG stationline (m) | Change in SLNCG (m) |
|---|---|---|---|
| 10 | 0.4144 | 0.3579 | 0.0547 |
| 30 | 0.5235 | 0.3579 | 0.1639 |
| 65 | 0.7147 | 0.3579 | 0.3550 |
| 95 | 0.8786 | 0.3579 | 0.5190 |

size, and the 10 per cent mass case now shows the greatest improvement. Therefore, the high mass percentage case's improvements over the highly stable round must be tempered by the low mass percentage case's improvements over the reduced stability round, and a mass percentage in between the two extremes would provide the best trade-off.

## 4 CONCLUSION

The variable stability mechanism has been developed to reduce required control forces for smart munitions, which often suffer from a lack of control authority. The results presented above demonstrate that a one-time shift in the mass centre location in flight enables optimization of projectile flight characteristics by reducing throw-off error and increasing control authority. An active control of a projectile's centre of gravity position using the variable stability mechanism lets the designer have the 'best of both worlds', that is a projectile with low susceptibility to initial throw-off errors and high control authority throughout controlled portions of flight. Trade studies performed using a seven-degree-of-freedom flight dynamic model show that projectiles equipped with a variable stability mechanism exhibit lower dispersion for a given maximum manoeuvre control force because of decreased initial errors and increased control authority. Increases in translating mass size result in less dispersion, although at some point no benefit is obtained by further increasing mass percentage. Flight dynamic and control improvements must be tempered by the fact that the control mechanism adds complexity, but probably more importantly claims space on the round that is in high demand.

© Authors 2009

## REFERENCES

1 **Rollstin, L. R.** Experimental determination of the artillery shell mass-property/trajectory-drift relationship. *J. Spacecr.*, 1978, **16**(2), 108–114.

2 **Soper, W.** Projectile instability produced by internal friction. *AIAA J.*, 1978, **16**(1), 8–11.

3 **Murphy, C.** Influence of moving internal parts on angular motion of spinning projectiles. *J. Guid. Control*, 1978, **1**(2), 117–122.

4 **D'Amico, W.** Comparison of theory and experiment for moments induced by loose internal parts. *J. Guid. Control*, 1987, **10**(1), 14–19.

5 **Hodapp, A.** Passive means for stabilizing projectiles with partially restrained internal members. *J. Guid. Control*, 1989, **12**(2), 135–139.

6 **Petsopoulos, T., Regan, F.,** and **Barlow, J.** Moving mass roll control system for fixed-trim re-entry vehicle. *J. Spacecr. Rockets*, 1996, **33**(1), 54–61.

7 **Robinett, R., Sturgis, B.,** and **Kerr, S.** Moving mass trim control for aerospace vehicles. *J. Guid. Control Dyn.*, 1996, **19**(5), 1064–1071.

8 **Menon, P., Sweriduk, G., Ohlmeyer, E.,** and **Malyevac, D.** Integrated guidance and control of moving mass actuated kinetic warheads. *J. Guid. Control Dyn.*, 2004, **27**(1), 118–127.

9 **Frost, G.** and **Costello, M.** Linear theory of a projectile with a rotating internal part in atmospheric flight. *J. Guid. Control Dyn.*, 2004, **27**(5), 898–906.

10 **Frost, G.** and **Costello, M.** Control authority of a projectile equipped with an internal unbalanced part. *J. Dyn. Syst. Meas. Control*, 2006, **128**(4), 1005–1012.

11 **Rogers, J.** and **Costello, M.** Control authority of a projectile equipped with an internal translating mass. *J. Guid. Control Dyn.*, 2008, **31**(5), 1323–1333.

12 **Slotine, J.** and **Li, W.** *Applied nonlinear control*, 1991, pp. 207–236 (Prentice-Hall, Inc., USA).

13 **Zarchan, P.** *Tactical and strategic missile guidance*, 2002, pp. 12–15 (American Institute of Aeronautics and Astronautics, Inc., USA).

## APPENDIX

### Notation

| | |
|---|---|
| $\vec{a}_{P/I}$ | translational acceleration of the projectile centre of mass with respect to the inertial frame |
| $\vec{a}_{T/I}$ | translational acceleration vector of the internal translating mass centre of mass with respect to the inertial frame |
| $\vec{A}_C$ | acceleration command generated by proportional navigation controller |
| $c_V$ | viscous damping coefficient in the sleeve for the internal translating mass |
| $C$ | point at centre of mass of composite projectile-translating mass system |
| $C_i$ | various projectile aerodynamic coefficients |
| $\mathbb{C}_X(y)$ | vector component operator that outputs a column vector comprised the components of the input vector $y$ expressed in reference frame X |
| CEP | radius of a circle centred at the mean impact point that encircles half the impact points in a dispersion simulation |
| $f_{Input}$ | scalar value of the input force exerted by the controller |
| $g$ | acceleration due to gravity ($9.81 \, \text{m/s}^2$) |
| $\vec{H}_{P/I}^P$ | angular momentum of the projectile with respect to the inertial frame about the projectile body mass centre |

| | |
|---|---|
| $\vec{H}_{T/I}^{T}$ | angular momentum of the internal translating mass with respect to the inertial frame about the internal translating mass centre |
| $I_I, J_I, K_I$ | inertial reference frame unit vectors |
| $I_L, J_L, K_L$ | line-of-sight frame unit vectors |
| $I_P, J_P, K_P$ | projectile reference frame unit vectors |
| $I_P$ | mass moment of inertia matrix of the projectile body with respect to the projectile reference frame |
| $I_T$ | mass moment of inertia matrix of the internal translating mass with respect to the projectile reference frame |
| ITM | internal translating mass |
| $m$ | total system mass |
| $m_P$ | projectile body mass |
| $m_T$ | internal translating mass |
| $\vec{M}^C$ | total external moment applied to the system about the system mass centre |
| $M_X, M_Y, M_Z$ | external moment components on the projectile body expressed in the projectile reference frame |
| $N_C$ | proportional navigation gain |
| $p, q, r$ | components of the angular velocity vector of the projectile body expressed in the projectile reference frame |
| $r_{C \rightarrow P}$ | distance vector from the centre of mass of the system to the projectile centre of mass |
| $r_{C \rightarrow T}$ | distance vector from the centre of mass of the system to the internal translating mass centre of mass |
| $r_{C \rightarrow X}$ | distance vector from the centre of mass of the system to the desired impact point |
| $r_{P \rightarrow T}$ | distance vector from the projectile centre of mass to the internal translating mass centre of mass |
| $r_{PA}$ | cavity offset from the projectile centre of mass |
| $s$ | position of the internal translating mass along its line of movement with respect to the centre of the cavity |

| | |
|---|---|
| $\mathbb{S}_X(y)$ | cross-product operator that outputs a skew-symmetric matrix using the components of the input vector $y$ expressed in reference frame X |
| SLNCG | stationline CG position referenced from the rear of the projectile |
| $\mathbf{T}_{IP}$ | transformation matrix from the inertial reference frame to the projectile reference frame |
| $u, v, w$ | translation velocity components of the composite body centre of mass resolved in the projectile reference frame |
| $v_{C/I}$ | velocity of the system mass centre with respect to the inertial frame |
| $v_{T/P}$ | velocity of the internal translating mass centre of mass with respect to the projectile reference frame |
| $v_S$ | magnitude of the velocity of the translating mass with respect to the translating mass reference frame |
| $V_C$ | missile-target closing velocity |
| $x, y, z$ | position vector components of the composite body centre of mass expressed in the inertial reference frame |
| $X_T$ | distance from the centre of the internal translating mass cavity to the system centre of mass |
| $X, Y, Z$ | total external force components on the composite body expressed in the projectile reference frame |
| $\theta_T, \psi_T$ | Euler pitch and yaw angles for the orientation of the line of movement of the internal translating mass with respect to the projectile body |
| $\lambda$ | line-of-sight angle between a vector from the projectile to the target and a vector along the projectile's axis of symmetry |
| $\phi, \theta, \psi$ | Euler roll, pitch, and yaw angles |
| $\vec{\omega}_{P/I}$ | angular velocity of the projectile body with respect to the inertial frame |
| $\vec{\omega}_{L/I}$ | angular velocity of the line-of-sight frame with respect to the inertial frame |